JOURNAL OF COMPUTATIONAL PHYSICS 49, 118–150 (1983)

Finite-Element Methods for Steady Solidification Problems

HISHAM M. ETTOUNEY AND ROBERT A. BROWN

Department of Chemical Engineering,
Massachusetts Institute of Technology, Cambridge, Massachusetts 02139

Received February 19, 1982

Four Galerkin finite-element methods are tested for solving the free-boundary problem that describes steady solidification. The formulations differ in the solution method used to account for the unknown shape of the melt/solid interface, in the interphase condition (either balance of heat flux or equilibrium of temperature) distinguished for locating the interface, and in the technique used for solving the systems of algebraic equations that result from the finite-element approximations. Methods that use the melting point isotherm to locate the melt/solid interface are found more accurate and efficient than formulations based on the interfacial energy balance. Solution by a Galerkin–Newton algorithm of the free-boundary problem transformed to a fixed domain is most efficient when the field problem in each phase is made nonlinear by including radiation from the melt and solid to the surroundings.

1. INTRODUCTION

Precise understanding of the physics that controls the shape of the phase boundary separating melt and solid during steady solidification is becoming increasingly important. For semiconductor crystals grown from the melt, the shape of the melt/solid interface influences both the density of crystallographic defects [1] and the uniformity of composition [2] in the crystal. The shape of this phase boundary is set by transport of heat and mass through melt and solid phases, across the interphase boundary, and to the surroundings. In general, fluid flow in the melt controls convective heat and mass transfer. The mathematical description of steady solidification is a two-phase free-boundary problem composed of a set of coupled partial differential equations and boundary conditions that are solved for the field variables (velocity, temperature, concentration, and pressure) as well as for the shape of the phase boundary. Nonlinearities appear in such a solidification model from both the coupling between the shape of the phase boundary and the field variables and from nonlinear (e.g., convective) terms in the field equations and in conditions imposed along fixed and free boundaries. The numerical methods discussed in this paper are focused on efficient and accurate solution of steady solidification problems with *both* types of nonlinearities.

Although many numerical methods have been proposed for solving two-dimensional moving- (time dependent) and free- (steady state) boundary problems,

0021-9991/83/010118–33$03.00/0

only a few have treated models which have nonlinearities in the field equations, such as arise from accounting for natural convection [3–5]. Most techniques [6–23] have been designed for Stefan-like problems where only one field variable, usually temperature, is present and the field equation is linear. In these algorithms the calculation of the temperature field and interface shape have been decoupled into successive steps. Once an interface shape has been assumed, either finite difference or finite element approximations reduce the energy equation and boundary conditions to a set of linear algebraic equations. The temperature field calculated as the solution to these equations is used to compute another approximation to the interface from one of the boundary conditions at the interface *distinguished* for this purpose. The iteration is repeated until it converges. Decoupling the calculation of the interface shape and field variables amounts to a successive approximation iteration that converges linearly [24]. Adding nonlinearities to the field equations complicates these iterations by making the equation set that describes the temperature field nonlinear and the solution of these equations iterative.

An alternative to successive approximations is to iterate simultaneously for the interface shape and field variables. Newton's method [24] is the most powerful scheme for doing this because it gives quadratic convergence. As is shown here, the rapid convergence of Newton's method compared to successive approximation techniques makes a profound difference in the efficiency of the algoritm, especially when the nonlinearities in the field equations cause multiple iteration loops. Also, the application of Newton's method leads to powerful techniques for computer-aided analysis of the sensitivity of the solution to parameters and of solution multiplicity [25]. To implement Newton's method requires computing the Jacobian matrix that describes the sensitivity of the residuals of the energy balance and boundary conditions to changes in the temperature field *and* interface location. The sensitivity of the residuals to changes in the interface shape involve changes in the grid used for the approximation and hence in the approximation itself.

We present four methods, each based on Galerkin finite-element analysis, for solving steady solidification problems. The four schemes are compared for a Stefan-like solidification problem presented in Section 2 where only heat transfer determines the shape of the phase boundary, which is assumed to be represented as a single-valued function of one spatial coordinate. This prototype problem arises as a model for the forming of thin silicon sheets by solidification of melt extruded through a die, a technique known as edge-defined film-fed growth [26–27]. Nonlinearities in this model arise from the unknown location of the melt/solid interface, from latent heat release at the interface, and from radiation of heat from the sides of the sheet to the ambient. This last nonlinearity affects only the discretized field equations and is a *simple* example of the type caused by fluid flow in the melt which serves there to point to differences between successive approximation and Newton iteration methods.

The finite element and finite difference methods developed previously for solving this type of free-boundary problem and the four new methods presented here are classified according to (i) the method used to account for the nonlinearity caused by the unknown interface, (ii) the condition, either interfacial equilibrium of temperature

or energy conservation, used as the *distinguished* boundary condition, and (iii) the method used to solve the set of nonlinear algebraic equations that result from the choices made in (i) and (ii).

Two boundary conditions are specified at the melt/solid interface. The first forces both melt and solid temperatures along the phase boundary to equal the equilibrium melting temperature of the material; the second balances the net flux by conduction through the interace with the latent heat released by solidification. Although both interfacial conditions (along with the energy balances and other boundary conditions) must be satisfied simultaneously by any solution, it is convenient in constructing numerical methods and asymptotic solutions to classify them. We shall consider one condition as an interphase boundary condition for the energy balances and the second condition will be *distinguished* for determining the location of the phase boundary. *This distinction seems arbitrary.* As is shown in this paper, however, the choice of *distinguished* condition strongly influences the rate of convergence and accuracy of a numerical solution to a free-boundary problem. Silliman and Scriven first pointed out this fact with respect to convergence of finite-element schemes for solving the free-boundary problem arising from the steady flow of a viscous liquid with a free surface [28].

Methods for handling the nonlinearity caused by the free boundary are categorized according to whether the numerical grid (either elements of difference points) is fixed in space [6–14] or deforms [15–23] to conform with the shape of the phase boundary. The enthalpy method [7–8] uses a regular finite-difference grid and locates the melt/solid interface only to within a grid block. Calculation of accurate shapes by this method requires fine grids and hence is prohibitively expensive for complicated problems.

More accurate approximations for interface shape are calculated with fixed grids when the original solidification problem is transformed so that melt and solid regions have fixed boundaries, of which the interface is one. The problem reduces to solving a coupled set of nonlinear partial differential equations, boundary conditions, and a *distinguished* condition, *all* written in terms of the temperature field and interface shape. This transformation technique was applied first by Landau [8] for one-dimensional and later by others [9–11] to two-dimensional Stefan problems where the inteface shape was a function of a single spatial coordinate. The Isotherm–Migration method [12–14] is a special case of the Landau transformation where temperature is interchanged with a spatial variable.

Previous applications of transformation methods [10–11] all solve the nonlinear equation set by successive iteration between the interface shape and the temperature field. As shown in Section 3, Newton's method is simply applied to this equation set because the dependence on the shape of the phase boundary is explicit in the transformed equations and all the terms of the Jacobian matrix are easily calculated in closed form.

Solution of the free-boundary problem in the original coordinate system has the additional complication of requiring the genration of a new, and generally irregular, grid at each iteration. Meyer [15–18] has developed finite difference methods based

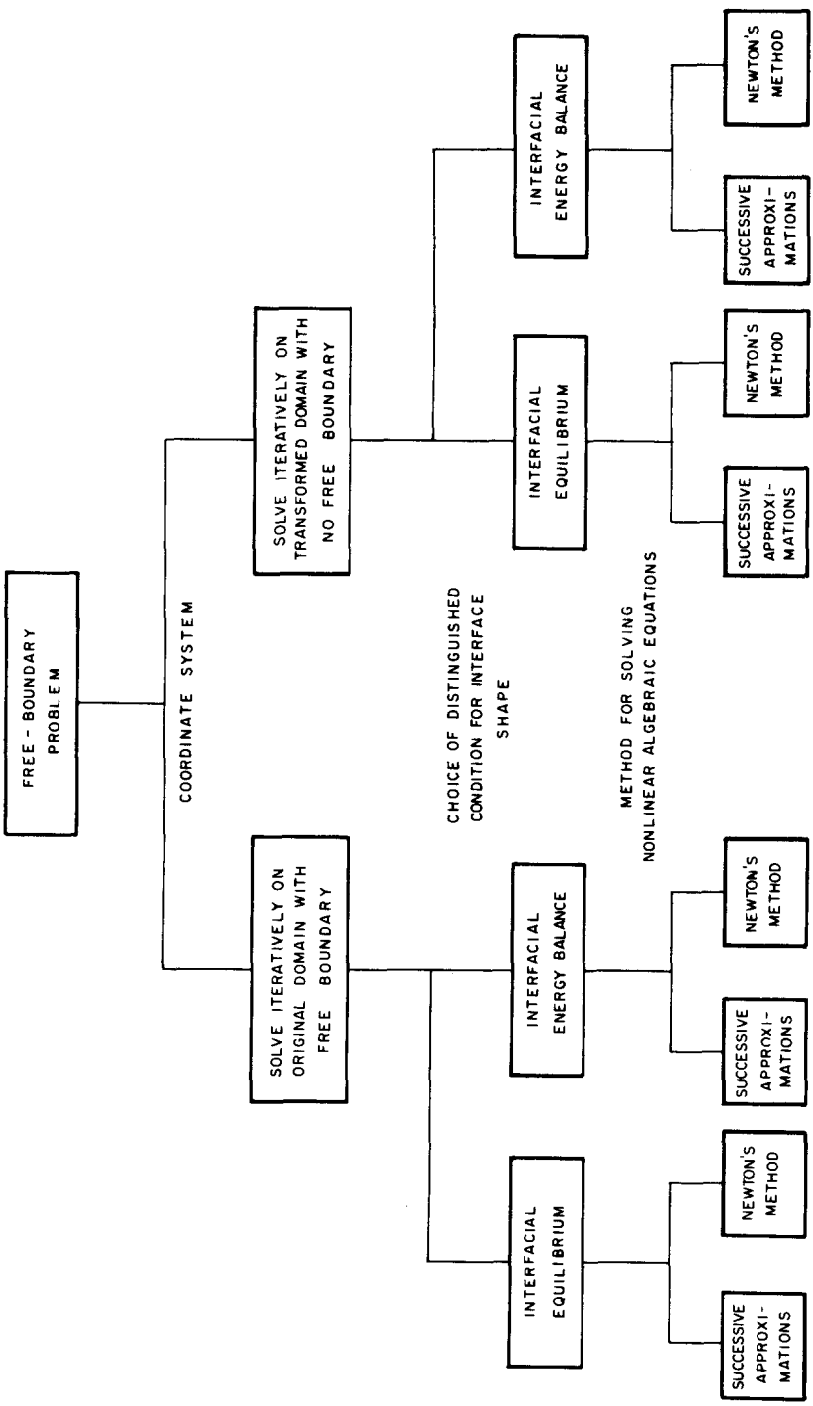

FIG. 1. Classification of methods for solving steady solidification problems. The Isotherm, Kinematic–Isotherm, Newton–Isotherm, and Energy–Flux methods are shown as formulations I, V, VI, and VIII, respectively.

on the method of lines for solving free-boundary and Stefan problems with linear field equations. Several finite element techniques have been proposed for moving elements in Stefan problems [19–23]; these are reviewed in [23]. Each of these methods integrates explicitly for the melt/solid interface location at each time step and avoids the problem of solving nonlinear algebraic equations. Finite element methods have not been applied previously to the steady solidification problem.

The classification of numerical methods for solving free-boundary problems is summarized in Fig. 1. The four finite element methods discussed in detail in Sections 3 are I, V, VI, and VIII. Comment about the viability of methods III and VII are also made. The accuracy and efficiency of the four schemes are compared in Section 4 for two cases, in terms of parameters, of the model problem. In the first, the nonlinearities caused by radiation and latent heat are removed and a closed form solution is known for comparing accuracy. In the second, extreme values of the Stefan (latent heat) and radiation numbers are used to demonstrate the rapid convergence of the algorithm based on Newton's method over wide ranges of parameters.

2. Model Solidification Problem

In edge-defined film-fed growth (EFG), a sheet of melt is extruded from a die at a constant rate V and solidified by transferring heat from the sheet to the surroundings. We assume that the die, melt, and solid sheet all have the same thickness $2b$ and that the sheet is so wide that heat transfer is the same across any longitudinal section of melt and solid. We analyze only one slice of the sheet; see Fig. 2.

Our heat transfer model for EFG is developed in [27] and is only presented here in dimensionless form. The half-thickness of the die b has been used as the characteristic length scale and temperature T_0 of the melt exiting from the die has been used as the characteristic temperature scale.

2.1 *Heat Transfer Problem*

A rectangular Cartesian coordinate system (x, y) is defined with its origin at the center of the sheet and in the plane of the die exit. The interface between melt and solid is located at $y = h(x)$ and the vector field $\mathbf{n}$ everywhere normal to this interface is

$$\mathbf{n} = (\mathbf{e}_y - \mathbf{e}_x h_x)/[1 + h_x^2]^{1/2}, \tag{1}$$

where $h_x \equiv \partial h/\partial x$ and $(\mathbf{e}_x, \mathbf{e}_y)$ are unit vectors in the x- and y-directions, respectively. The vectors normal to other boundaries are shown on Fig. 2.

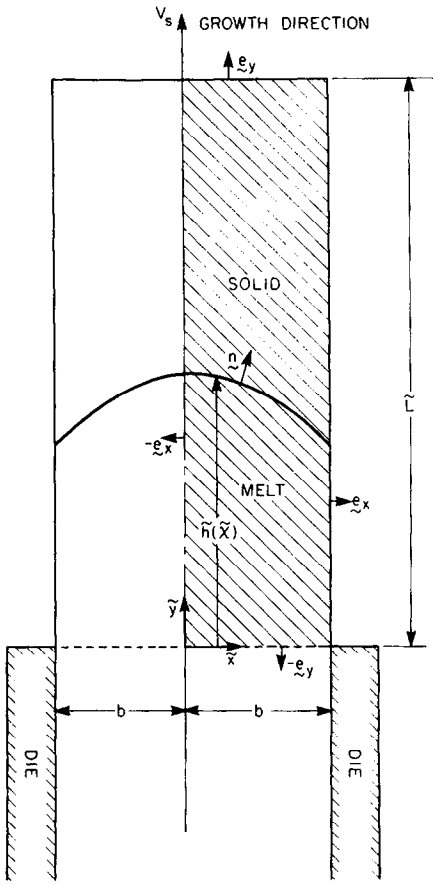

FIG. 2. Model of edge-defined film-fed growth (EFG). Computational domain is marked by (\\\\).

To simplify the thermal model, we set the thermal and physical properties, i.e., density ρ, thermal conductivity k, heat capacity c_p, heat transfer coefficient h, and emissivity ε, of melt and solid equal. The dimensionless energy balances in melt ($i = \ell$) and solid ($i = s$) are

$$\nabla \cdot \nabla T_i - P(\mathbf{e}_y \cdot \nabla T_i) = 0, \qquad i = \ell, s, \qquad 0 \leqslant y \leqslant L, \quad 0 \leqslant x \leqslant 1. \tag{2}$$

The Peclet number $P \equiv V\rho c_p b/k$ measures the importance of heat transfer by convection in the growth direction relative to conduction across the sheet. The melt and solid occupy regions $\mathscr{D}_\ell$ and $\mathscr{D}_s$, respectively, as shown in Fig. 3.

At the phase boundary ($y = h(x)$, $0 \leqslant x \leqslant 1$) the interfacial energy balance

$$\mathbf{n} \cdot \nabla T_\ell - \mathbf{n} \cdot \nabla T_s = PS(\mathbf{n} \cdot \mathbf{e}_y) \tag{3}$$

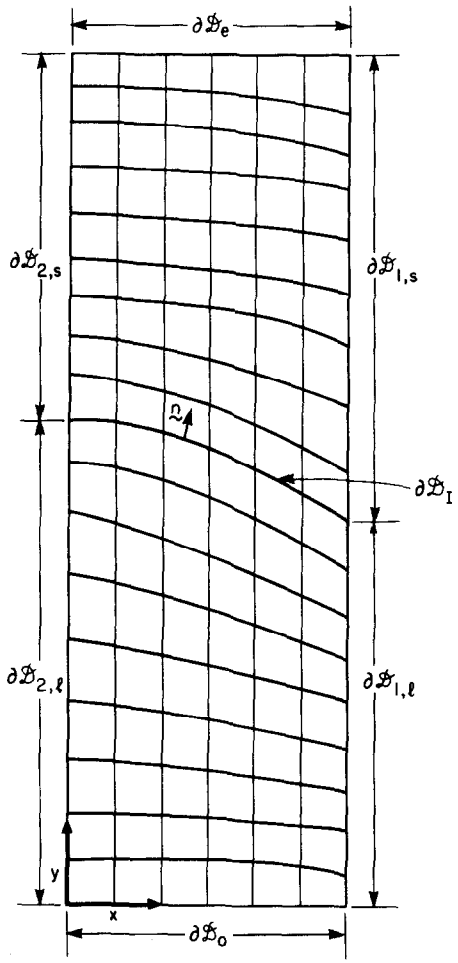

FIG. 3. Sample finite-element discretization in original coordinate system. The melt/solid interface is the mesh curve denoted as the boundary $\partial\mathscr{D}_I$. The notation for other boundaries is also shown.

and the conditions for thermal equilibrium

$$T_s(x, h(x)) = T_\ell(x, h(x)) = T_m \tag{4}$$

must be met. The dimensionless melting temperature is T_m and the Stefan number is $S \equiv \Delta H_f / c_p T_0$, where ΔH_f is the latent heat of fusion. Heat transfer from melt and solid to the surroundings at temperature T_∞ is by both convection and radiation,

$$-\partial T_i/\partial x = B(T_i - T_\infty) + R(T_i^4 - T_\infty^4), \qquad i = \ell, s, \quad x = 1, \quad 0 \leqslant y \leqslant L. \tag{5}$$

The Biot number $B \equiv hb/k$ and radiation number $R \equiv \sigma\varepsilon bT_0^3/k$ (σ is the Stefan–Boltzmann constant) measure the efficiencies of heat losses from the sheet by convection and radiation relative to conduction across the thickness of the sheet. These two dimensionless numbers control the amount of heat lost laterally from the sheet and hence control the curvature of the phase boundary.

The midplane of the sheet is assumed to be a plane of reflective symmetry

$$\partial T_i/\partial x = 0, \qquad i = \ell, \ s, \quad x = 0, \quad 0 < y < L, \tag{6}$$

and the temperatures at the die exit ($y = 0$) and at the end of the solid ($y = L$) are fixed at constant values,

$$T_\ell(x, 0) = 1, \qquad T_s(x, L) = T_e, \qquad 0 \leqslant y \leqslant 1. \tag{7}$$

Equations (2–7) define a mathematical free-boundary problem for the temperature fields in melt and solid and the shape of the melt/solid interface. The equation set is nonlinear because of the coupling between $h(x)$ and the temperature fields through boundary condition (3) and because of the quartic dependence on temperature in boundary condition (5) caused by radiation from the sheet. Allowing the material properties to differ in the melt and solid causes other nonlinearities; in this case, the form of energy balance (2) to be satisfied depends on the location of the phase boundary $h(x)$.

A closed-form solution of equation set (2–7) is known only when all nonlinearities are removed; this is the case when radiation ($R = 0$) and latent heat ($S = 0$) are neglected. Then the problem reduces to heat transfer in a moving sheet of a single material and the temperature field is calculated by separation of variables techniques [29]. The isotherms for this case are shown in Fig. 4 for the variables $T_e = T_\infty = 0$, $L = 1$, $B = 1$, $P = 0.5$, and the isotherm $T_m = 0.5$ designated as the melt/solid interface. This case is used as an initial base for comparison of the four finite-element algorithms.

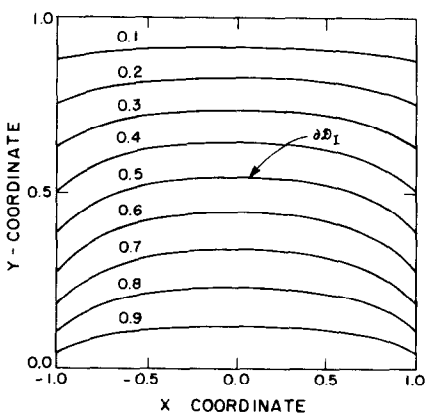

FIG. 4. Isotherms for prototype solidification problem; $P = 0.5$, $B = 1.0$, and $T_m = 0.5$.

2.2 *Transformation to Regions with Known Boundaries*

To make explicit the nonlinearities caused by the unknown shape of the melt/solid interface, the free-boundary problem of Eqs. (2)–(7) is mapped to the coordinate systems (ξ, n) in melt and $(\hat{\xi}, \hat{n})$ in solid as shown in Fig. 5. The melt/solid interface has known shape in the transformed coordinate systems; melt occupies the region $\hat{\mathscr{D}}_\ell (0 \leqslant \xi \leqslant 1, \quad 0 \leqslant \eta \leqslant L/2)$ and solid occupies the region $\hat{\mathscr{D}}_s (0 < \hat{\xi} < 1, L/2 \leqslant \hat{\eta} \leqslant L)$. The relationships between the transformed coordinates and the original coordinates are

$$\text{melt:} \quad \xi \equiv x, \qquad \eta \equiv yL/2h(x), \tag{8}$$

$$\text{solid:} \quad \hat{\xi} \equiv x, \qquad \hat{\eta} \equiv [1 - (1/2)(L - y)/(L - h(x))]L. \tag{9}$$

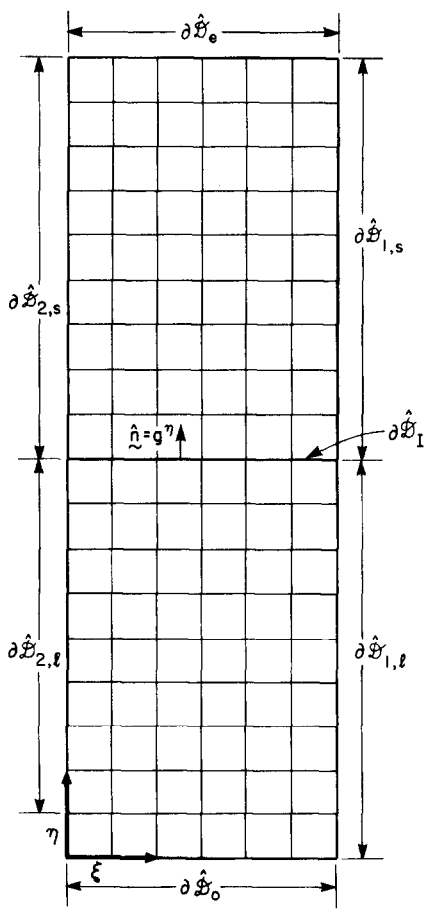

FIG. 5. Sample finite-element mesh in transformed coordinates.

The transformed coordinates ξ and $\hat{\xi}$ are identical and will be used interchangeably. Equations (8) and (9) define nonorthogonal coordinate systems in melt and solid. To preserve the gradient form of energy balances (2) and boundary conditions (3) during the change of coordinates, the operator ∇ must be expressed in these coordinates. The base vectors associated with the transformed coordinate systems are introduced as $(\mathbf{g}_\xi, \mathbf{g}_\eta)$ for the melt and $(\hat{\mathbf{g}}_\xi, \hat{\mathbf{g}}_\eta)$ for the solid.

$$\text{melt:} \quad \mathbf{g}_\xi \equiv \mathbf{e}_x + (2h_\xi \eta/L)\,\mathbf{e}_y, \tag{10a}$$

$$\mathbf{g}_\eta \equiv (2h(\xi)/L)\,\mathbf{e}_y, \tag{10b}$$

$$\text{solid:} \quad \hat{\mathbf{g}}_{\hat{\xi}} \equiv \mathbf{e}_x + 2h_{\hat{\xi}}(1 - \hat{\eta}/L)\,\mathbf{e}_y, \tag{11a}$$

$$\hat{\mathbf{g}}_{\hat{\eta}} \equiv (2/L)(L - h(\hat{\xi}))\,\mathbf{e}_y. \tag{11b}$$

The reciprocal base vectors are [30]

$$\text{melt:} \quad \mathbf{g}^\xi \equiv \mathbf{e}_x, \tag{12a}$$

$$\mathbf{g}^\eta \equiv (L\mathbf{e}_y - 2h_{\hat{\xi}}\eta\mathbf{e}_x)/2h(\xi), \tag{12b}$$

$$\text{solid:} \quad \hat{\mathbf{g}}^{\hat{\xi}} \equiv \mathbf{e}_x, \tag{13a}$$

$$\hat{\mathbf{g}}^{\hat{\eta}} \equiv (L\mathbf{e}_y - 2h_{\hat{\xi}}(L - \hat{\eta})\,\mathbf{e}_x)/2(1 - h(\hat{\xi})). \tag{13b}$$

The gradients of temperature in melt $\hat{\nabla}_\ell \hat{T}_\ell$ and solid $\hat{\nabla}_s \hat{T}_s$ in transformed coordinates are simply

$$\text{melt:} \quad \hat{\nabla}_\ell \hat{T}_\ell \equiv \mathbf{g}^\xi \frac{\partial \hat{T}_\ell}{\partial \xi} + \mathbf{g}^\eta \frac{\partial \hat{T}_\ell}{\partial \eta} = \mathbf{e}_x \left[\frac{\partial \hat{T}_\ell}{\partial \xi} - \frac{h_\xi \eta}{h} \frac{\partial \hat{T}_\ell}{\partial \eta} \right] + \mathbf{e}_y \left(\frac{L}{2h} \right) \frac{\partial \hat{T}_\ell}{\partial \eta}, \tag{14}$$

$$\text{solid:} \quad \hat{\nabla}_s \hat{T}_s \equiv \hat{\mathbf{g}}^{\hat{\xi}} \frac{\partial \hat{T}_s}{\partial \hat{\xi}} + \hat{\mathbf{g}}^{\hat{\eta}} \frac{\partial \hat{T}_s}{\partial \hat{\eta}} = \mathbf{e}_x \left[\frac{\partial \hat{T}_s}{\partial \hat{\xi}} - \frac{h_{\hat{\xi}}(L - \hat{\eta})}{(L - h)} \frac{\partial \hat{T}_s}{\partial \hat{\eta}} \right] + \mathbf{e}_y \left[\frac{L}{2(L - h)} \right] \frac{\partial \hat{T}_s}{\partial \hat{\eta}}. \tag{15}$$

Energy balances (2) can be written in transformed coordinates by formulating the Laplacian $\hat{\nabla}_i^2 \hat{T}_i \equiv \hat{\nabla}_i \cdot \hat{\nabla}_i \hat{T}_i$ using the definition of the gradient operators given above. This is not done here since Galerkin's method does not require the computation of $\hat{\nabla}_i^2 \hat{T}_i$. It is obvious from Eq. (14) and (15) that the energy balances written in transformed coordinates are nonlinear functions of the unknown shape of the melt/solid interface $h(\xi)$. These nonlinearities are caused solely by the free-boundary problem and are present even when radiative heat transfer is neglected ($R = 0$).

The relationships between the differential element of area in the original coordinate system $dA \equiv dx\,dy$ and the elements of area in the transformed regions are calculated

in terms of determinants g_ℓ and g_s of the metric tensors [30] associated with coordinate transformations (8) and (9);

$$\text{melt:} \quad dA \equiv g_\ell^{1/2}\, d\xi\, d\eta = 2h/L\, d\xi\, d\eta, \tag{16a}$$

$$\text{solid:} \quad dA \equiv g_s^{1/2}\, d\xi\, d\hat{\eta} = 2(1 - (h/L))\, d\xi\, d\hat{\eta}. \tag{16b}$$

3. Finite-Element Analysis

The Galerkin finite-element method forms the framework of the four techniques developed here for solving the steady solidification problem of Eqs. (2)–(7). In each algorithm the temperature fields $T_\ell(x, y)$ and $T_s(x, y)$ and interface location $h(x)$ are represented in expansions of finite-element basis functions and unknown coefficients such as

$$T_\ell(x, y) = \sum_{i=1}^{N_\ell} \alpha_{i,\ell}\, \Phi^i(x, y), \qquad T_s(x, y) = \sum_{i=1}^{N_s} \alpha_{i,s} \Phi_i(x, y), \tag{17a}$$

$$h(x) = \sum_{i=1}^{M} \beta_i\, \Psi^i(x), \tag{17b}$$

where N_ℓ, N_s, and M are the numbers of basis functions associated with unknown coefficients in each expansion. Bilinear and reduced quadratic polynomials [31] are tested here as bases $\{\Phi^i(x, y)\}$ for representing temperature and the corresponding linear and quadratic polynomials are used for representing melt/solid interface shape $\{\Psi^i(x)\}$.

The coefficients $\{\alpha_{i,\ell}, \alpha_{i,s}\}$ are determined by forcing to zero the set of Galerkin weighted residual equations formed from energy balances (2) and the boundary conditions. The coefficients $\{\beta_i\}$ in the expansion for melt-solid interface shape are determined by satisfying the chosen *distinguished* condition, either (3) or (4).

The a priori unknown shape of the phase boundary complicates the finite-element expansions (or any other discretization) when the original coordinate system is used. During numerical iteration any change in the location of the interface requires that the position of the quadrilateral mesh be changed (see Fig. 3) and that the finite-element basis be regenerated. The Isotherm method updates the mesh and basis at each iteration. The condition for interfacial equilibrium (4) is used as the *distinguished* condition; see Fig. 1. An alternative approach which circumvents the regeneration of the mesh and finite-element basis at each iteration is to solve the solidification problem in the transformed coordinates defined by Eqs. (8 and 9). In these coordinates, a fixed finite-element grid is established (see Fig. 5) and the nonlinear coupling between the temperature field and interface shape is set. The Kinematic–Isotherm, Isotherm–Newton, and Energy–Flux methods all solve problem (2)–(7) in transformed coordinates. As shown in Fig. 1, these methods differ in the choice of *distinguished* condition, either (3) or (4), and the iterative method used to

solve the system of nonlinear algebraic equations. Each finite-element algorithm is outlined below.

3.1 *Solution in Original Coordinates: Isotherm Method*

When the condition for interfacial equilibrium is used as the *distinguished* condition, the finite-element representations for the temperature fields are most conveniently combined into a single field as

$$T_j(x,y) = \sum_{i=1}^{N_\ell} a_{i,j}\Phi^i(x,y) + \sum_{i=1}^{N_s} a_{i,j}\Phi^i(x,y) + \sum_{i=1}^{N_0} a^e_{i,\ell}\,\Phi^i(x,y) + \sum_{i=1}^{N_e} a^e_{i,s}\Phi^i(x,y), \tag{18}$$

where N_0 is the number of basis functions defined at $y=0$, N_ℓ is the remaining number of functions defined in the melt, N_e is the number of basis functions defined at $y=L$, and N_s is the remaining number of functions defined in the solid. The nodes defining the temperature along the melt/solid interface are not separated out here, but are included in the set for the melt. Since the temperatures along the inlet and outlet boundaries are set by Eq. (7), the coefficients $\{a^e_{i,\ell}\}$ and $\{a^e_{i,s}\}$ are known. In the notation of Eq. (20), $T_j(x,y)$ is equal to $T_\ell(x,y)$ when the point (x,y) is in the melt and to $T_s(x,y)$ when (x,y) is in the solid. The Galerkin weighted residual integrals of Eqs. (2) are combined as a single integral over the total area $(\mathscr{D}_\ell + \mathscr{D}_s)$ of melt and solid and integrated by parts in the usual way to incorporate the flux boundary condition at the melt/solid interface. The residual equations that result are

$$\begin{aligned} R_j^{(I)} = &-\int_{\mathscr{D}_t} [\nabla T_i \cdot \nabla\Phi^j + P(\mathbf{e}_y \cdot \nabla T_i)\,\Phi^j]\,dA + \int_{\partial\mathscr{D}_\ell} \frac{\Phi^j PS}{[1+h_x^2]^{1/2}}\,d\ell \\ &-\int_{\partial\mathscr{D}_{1,\ell}} \Phi^j[B(T_\ell - T_\infty) + R(T_\ell^4 - T_\infty^4)]\,d\ell \\ &-\int_{\partial\mathscr{D}_{1,s}} \Phi^j[B(T_s - T_\infty) + R(T_s^4 - T_\infty^4)]\,d\ell = 0, \end{aligned} \tag{19}$$

$j = 1,\ldots, N_t$, where $N_t \equiv N_\ell + N_s$. The notation for boundaries displayed in Fig. 3 has been used and $d\ell$ is the increment of arc-length along each segment of boundary; $d\ell \equiv [1+h_x^2]^{1/2}\,dx$ along the phase boundary and $d\ell \equiv dy$ along the side of the sheet. Boundary conditions (5) and (6) and the fact that each basis function $\{\Phi^j\}$ vanishes on the boundaries $\partial\mathscr{D}_0$ and $\partial\mathscr{D}_e$ have also been used.

Equations (19) are a nonlinear algebraic set for the coefficients $\{\alpha_{i,\ell}, \alpha_{i,s}\}$ once the finite-element approximations for interface shape and temperature fields (17) are introduced and the area integrals are computed with nine-point Gaussian quadrature. This set is more conveniently expressed as

$$\mathbf{R}^{(I)}(\boldsymbol{\alpha}_\ell, \boldsymbol{\alpha}_s; \boldsymbol{\beta}^{(k)}) = \mathbf{0}, \tag{20}$$

where $\boldsymbol{\alpha}_\ell \equiv (\alpha_{1,\ell}, \alpha_{2,\ell}, \ldots, \alpha_{N_\ell,\ell})^T$, $\boldsymbol{\alpha}_s \equiv (\alpha_{1,s}, \alpha_{2,s}, \ldots, \alpha_{N_s,s})^T$, $\boldsymbol{\beta}^{(k)} \equiv (\beta_1^{(k)}, \beta_2^{(k)}, \ldots, \beta_M^{(k)})^T$. Equation set (20) is solved by Newton's method. From first approximations $(\boldsymbol{\alpha}_\ell^{(0)}, \boldsymbol{\alpha}_s^{(0)})$ to the temperature fields, successive refinements are calculated as solutions of the following linear equations at the mth iteration

$$\begin{pmatrix} \underline{\underline{J}}^{(\ell)} & \underline{\underline{0}} \\ \underline{\underline{0}} & \underline{\underline{J}}^{(s)} \end{pmatrix} \begin{pmatrix} \boldsymbol{\alpha}_\ell^{(m)} - \boldsymbol{\alpha}_\ell^{(m+1)} \\ \boldsymbol{\alpha}_s^{(m)} - \boldsymbol{\alpha}_s^{(m+1)} \end{pmatrix} = -\mathbf{R}^{(I)}(\boldsymbol{\alpha}_\ell^{(m)}, \boldsymbol{\alpha}_s^{(m)}; \boldsymbol{\beta}^{(k)}), \tag{21}$$

where the submatrices $\underline{\underline{J}}^{(\ell)}$ and $\underline{\underline{J}}^{(s)}$ have components $J_{ij}^{(\ell)} \equiv \partial R_i^{(I)}/\partial \alpha_{j,\ell}$ and $J_{ij}^{(s)} \equiv \partial R_i^{(I)}/\partial \alpha_{j,s}$, respectively. The Newton iterations are continued until the largest change in any element of the solution vector is smaller than 10^{-13}.

The temperature fields calculated as the solution of Eqs. (20) are not necessarily a solution of steady solidification problem (2)–(7). The latter is true only if the selected interface shape is the melting-point isotherm of the computed temperature distributions, that is, if $h(x)$ expressed by (17b) satisfies distinguished boundary condition (4). The melting point isotherm is interpolated linearly from (17b) with $y = h(x) = \sum_{j=1}^{M} \beta_j^{(k+1)} \psi^j(x)$. If the new coefficients $\{\beta_j^{(k+1)}\}$ calculated from the interpolation do not agree with the original estimate $\{\beta_j^{(k)}\}$ to one part in 10^{-13}, the entire

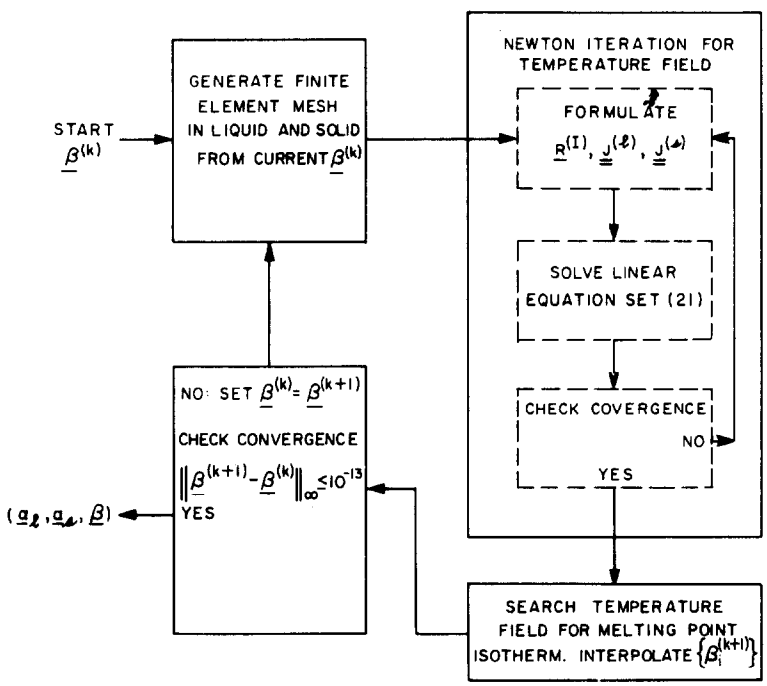

FIG. 6. Flowsheet for Isotherm method.

sequence is repeated using the new approximation $\{\beta_j^{k+1}\}$ in the temperature field calculation. The Isotherm formulation is shown schematically in Fig. 6. As discussed in Section 4, this iteration scheme has been found to converge for a wide range of values of Stefan and radiation numbers and initial approximations to interface shape $h(x)$.

The formulation marked as III on Fig. 1 was also tested. For an approximate interface shape, temperature fields were calculated that satisfied Eqs. (2) and (4)–(7). A new interface shape was found by solving by Newton's method the nonlinear equation set resulting from the Galerkin weighted residuals found from the interfacial energy balance, where the temperature gradients were evaluated from the previously calculated temperature field. The Jacobian matrix of the interface residual equations was numerically singular; consequently, the iteration for the new interface location diverged.

3.2 *Solution in Transformed Coordinates*

When the solidification problem is cast in the new coordinates of Eqs. (8) and (9), no free boundary exists. In a numerical solution scheme, there is no need for updating the finite element mesh as is necessary in the Isotherm method. Three numerical algorithms, the Kinematic–Isotherm, Isotherm–Newton, and Energy–Flux methods, are presented here in transformed coordinates. The choice of *distinguished* condition and the technique used to solve the nonlinear equation set are shown in Fig. 1 for each method.

3.2a *Kinematic–Isotherm Method*

When condition (4) for the melting point isotherm is used as the distinguished condition, the finite-element representation for the temperature fields $\hat{T}_j(\xi, \eta)$ in transformed regions for melt ($j = \ell$) and solid ($j = s$) are combined into a single field as

$$\hat{T}_j(\xi, \eta) = \sum_{i=1}^{N_\ell} \alpha_{i,\ell}\, \Phi^i(\xi, \eta) + \sum_{i=1}^{N_0} \alpha_{i,\ell}^e\, \Phi^i(\xi,\eta) + \sum_{i=1}^{N_s} \alpha_{i,s}\, \Phi^i(\xi, \eta) + \sum_{i=1}^{N_e} \alpha_{i,s}^e \Phi^i(\xi, \eta), \tag{22a}$$

and the interface shape is represented as

$$h(\xi) = \sum_{i=1}^{M} \beta_i \psi^i(\xi). \tag{22b}$$

The finite-element basis functions are defined in (ξ, η) coordinates with respect to a fixed grid (cf. Fig. 5). The Galerkin equations are formed by integrating the

transformed energy balances over the total area $\hat{\mathscr{D}}_t \equiv \hat{\mathscr{D}}_\ell + \hat{\mathscr{D}}_s$. Applying the transformed versions of boundary conditions (3), (5), and (6) yields

$$R_j^{(k)} \equiv -\tfrac{1}{2}\int_{\partial\hat{\mathscr{D}}_I} \Phi^j PS\, d\xi + \int_{\partial\hat{\mathscr{D}}_{1,\ell}} \Phi^j[B(\hat{T}_\ell - T_\infty) + R(\hat{T}^4 - T_\infty^4)](2h/L)\, d\eta$$

$$+ \int_{\partial\hat{\mathscr{D}}_{1,s}} \Phi^j[B(\hat{T}_s - T_\infty) + R(\hat{T}_s - T_\infty)](2/L)(L-h)\, d\hat{\eta}$$

$$+ \int_{\hat{\mathscr{D}}_t} [\hat{\nabla}_i \Phi^j \cdot \hat{\nabla}_i \hat{T}_k + \Phi^j Pe_y \cdot \nabla_i \hat{T}_i]\, g_i\, d\xi\, d\eta = 0, \qquad i = \ell, s,\ \ j = 1,\ldots, N_t. \tag{23}$$

The notation used for boundaries is shown in Fig. 5.

Substituting Eqs. (22) into Eqs. (23) gives a set of nonlinear algebraic equations in terms of the coefficients $\{\alpha_{i,\ell}\}$, $\{\alpha_{i,s}\}$, and $\{\beta_i\}$. The coefficients $\{\beta_i\}$ are determined by the M conditions that result from the constraints of interfacial equilibrium (4), the distinguished condition. The resulting set of $(N_t + M)$ nonlinear equations are explicit in the unknown coefficients and hence can be solved by any conventional method. We test two alternatives. The first, the Kinematic–Isotherm method, is a successive approximation scheme that decouples the $(N_t + M)$-dimensional set into N_t-dimensional set (23) for the temperature field and an auxiliary system of dimension M for determining interface shape. This splitting technique is akin to the Isotherm formulation. The second technique, the Isotherm–Newton method, solves the entire equation set by Newton's method.

In the first iteration of the Kinematic–Isotherm method, values of the coefficients $\{\beta_j^{(k)}\}$ are assumed and Eqs. (23) are reduced to a set of nonlinear algebraic equations in terms of the coefficients $\{\alpha_{i,\ell}\}$, $\{\alpha_{i,s}\}$:

$$\mathbf{R}^{(k)}(\boldsymbol{\alpha}_\ell, \boldsymbol{\alpha}_s; \boldsymbol{\beta}^{(k)}) = \mathbf{0}. \tag{24}$$

These equations are solved by Newton's method. The linear equation set solved at the mth iteration is

$$\underline{\underline{\hat{J}}}^{(K)} \begin{pmatrix} \hat{\boldsymbol{\delta}}_\ell^{(m)} \\ \hat{\boldsymbol{\delta}}_s^{(m)} \end{pmatrix} \equiv \begin{pmatrix} \underline{\underline{\hat{J}}}^{(\ell)} & \underline{\underline{0}} \\ \underline{\underline{0}} & \underline{\underline{\hat{J}}}^{(s)} \end{pmatrix} \begin{pmatrix} \boldsymbol{\alpha}_{(\ell)}^{(m)} - \boldsymbol{\alpha}_{(\ell)}^{(m+1)} \\ \boldsymbol{\alpha}_{(s)}^{(m)} - \boldsymbol{\alpha}_{(s)}^{(m+1)} \end{pmatrix} = -\mathbf{R}^{(m)}(\boldsymbol{\alpha}_t^{(m)}, \boldsymbol{\alpha}^{(m)}; \boldsymbol{\beta}^{(k)}), \tag{25}$$

were $\hat{J}_{ij}^{(\ell)} \equiv \partial R_i^{(m)}/\partial \alpha_{j,l}$ and $J_{ij}^{(s)} \equiv \partial R_i^{(m)}/\partial \alpha_{j,s}$.

The temperature field calculated as the solution of Eqs. (24) is only a solution of the solidification problem if the boundary $\eta = L/2$ is the melting point isotherm, that is, if transformed distinguished condition (4) is satisfied. Equation (4) is put in a new form by taking the derivative of the melt temperature in the direction always tangent to the melt/solid interface. From Eq. (4), the temperature does not vary in this direction. This condition is written in transformed coordinates as

$$\frac{dh^{(k+1)}}{d\xi} = \frac{dh^{(k)}}{d\xi} - \left(\frac{\partial \hat{T}_\ell/\partial \xi}{\partial \hat{T}_\ell/\partial \eta}\right)_{\eta = L/2} \left(\frac{2h^{(k)}}{L}\right), \tag{26}$$

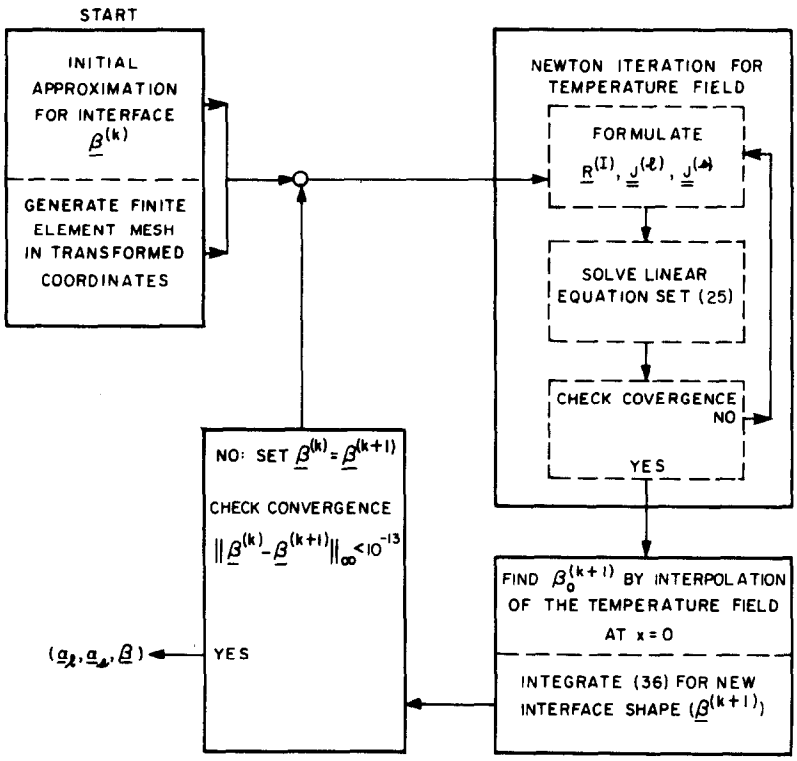

FIG. 7. Flowsheet for Kinematic–Isotherm method.

an identity when the interface between two successive iterations is identically an isotherm. All terms on the right-hand side of (26) are evaluated based on the previous approximation for $h^{(k)}(\xi)$ and the updated interface $h^{(k+1)}(\xi)$ is calculated by solving (26) by Euler's method. The initial condition $h^{(k+1)}(0)$ for the integration is determined so that the corresponding value of η (or $\hat{\eta}$) satisfies $T_i(0, \eta) = T_m$; this condition guarantees that the integration of (26) tracks the melting point isotherm.

The sequence of temperature field and interface shape calculations is repeated until the largest change of any coefficient $\{\beta_i^{(k)}\}$ for the interface is less than 10^{-13}. The Kinematic–Isotherm formulation is shown schematically in Fig. 7.

3.2b *Isotherm–Newton Method*

In this algorithm the $(N_t + M)$-dimensional equations formed from Eqs. (24) and *distinguished* condition (4) are solved by Newton's method. The M-dimensional form of the condition for the melting point is developed by equating the melt temperature $T_\ell(\xi, L/2)$ to T_m at each of the nodal points along the phase boundary (cf. Fig. 5)

$$R_{I,J}^N \equiv \hat{T}_\ell(\xi_j, L/2) - T_M = 0, \qquad j = 1,..., M. \tag{27}$$

The residual equations for the energy balances are taken as functions of $\{\beta_j\}$ as well as of $\{\alpha_{l,\ell}\}$ and $\{\alpha_{l,\sigma}\}$, i.e.,

$$\mathbf{R}_B^{(N)}(\boldsymbol{\alpha}_\ell, \boldsymbol{\alpha}_\sigma; \boldsymbol{\beta}) = \mathbf{R}^{(K)}(\boldsymbol{\alpha}_\ell, \boldsymbol{\alpha}_\sigma; \boldsymbol{\beta}). \tag{28}$$

The combined equation set (27)–(28) is partially coupled; the interface shape $h(x)$ appears in each of the residual equations (28). The distinguished conditions (27), however, are independent of the interface location $\{\beta_l\}$.

At each iteration a linear system of equations is solved

$$\underline{\underline{\hat{J}}}^{(N)} \boldsymbol{\Delta}^{(k+1)} \equiv \begin{pmatrix} \underline{\underline{\hat{J}}}^{(K)} & \underline{\underline{M}}^{(K)} \\ \cdots & \end{pmatrix} \begin{pmatrix} \boldsymbol{\alpha}_\ell^{(k)} - \boldsymbol{\alpha}_\ell^{(k+1)} \\ \boldsymbol{\alpha}_\sigma^{(k)} - \boldsymbol{\alpha}_\sigma^{(k+1)} \end{pmatrix} = \begin{pmatrix} \mathbf{R}_B^{(N)} \\ \cdots \end{pmatrix} \equiv \mathbf{R}^{(N)}, \tag{29}$$

where $\underline{\underline{\hat{J}}}^{(K)}$ is the N_t-dimensional Jacobian defined by Eq. (25) and the other submatrices are given by

$$M_{ij}^{(K)} \equiv \partial R_{B,i}^{(N)} / \partial \beta_j, \qquad i = 1,..., N_t, \qquad j = 1,..., M, \tag{30a}$$

$$L_{\ell,ij}^{(K)} \equiv \partial R_{I,i}^{(N)} / \partial \alpha_{\ell,j}, \qquad i = 1,..., M, \qquad j = 1,..., N_\ell, \tag{30b}$$

$$L_{\sigma,ij}^{(K)} \equiv \partial R_{I,i}^{(N)} / \partial \alpha_{\sigma,j}, \qquad i = 1,..., M, \qquad j = 1,..., N_\sigma, \tag{30c}$$

which are derived explicitly. The Jacobian $\underline{\underline{\hat{J}}}^{(N)}$ is sparse; the $(N_t \times N_t)$ portion $\underline{\underline{\hat{J}}}^{(K)}$ is tightly banded along its main diagonal. The last M columns and rows of $\underline{\underline{\hat{J}}}^{(N)}$ are not banded, so $\underline{\underline{\hat{J}}}^{(N)}$ has the "arrowhead" structure shown in Fig. 8. For the finite-element meshes considered below, the number of nonzero elements of $\underline{\underline{\hat{J}}}^{(N)}$ are evenly divided between the main submatrix $\underline{\underline{\hat{J}}}^{(K)}$ and the auxiliary matrices $\underline{\underline{M}}^{(K)}$, $\underline{\underline{L}}_\ell^{(K)}$, and $\underline{\underline{L}}^{(K)}$. A Fortran subroutine was written to perform Gaussian elimination on the system of

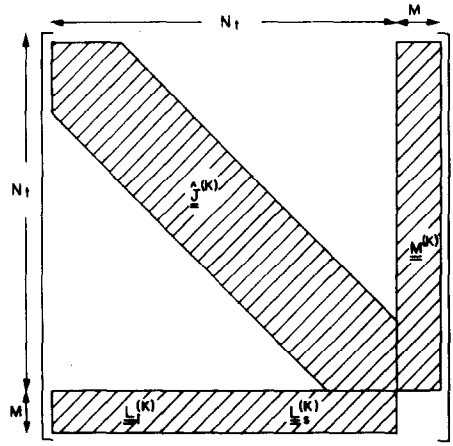

FIG. 8. Structure of Jacobian matrix $\underline{\underline{\hat{J}}}^{(N)}$ of Isotherm–Newton formulation.

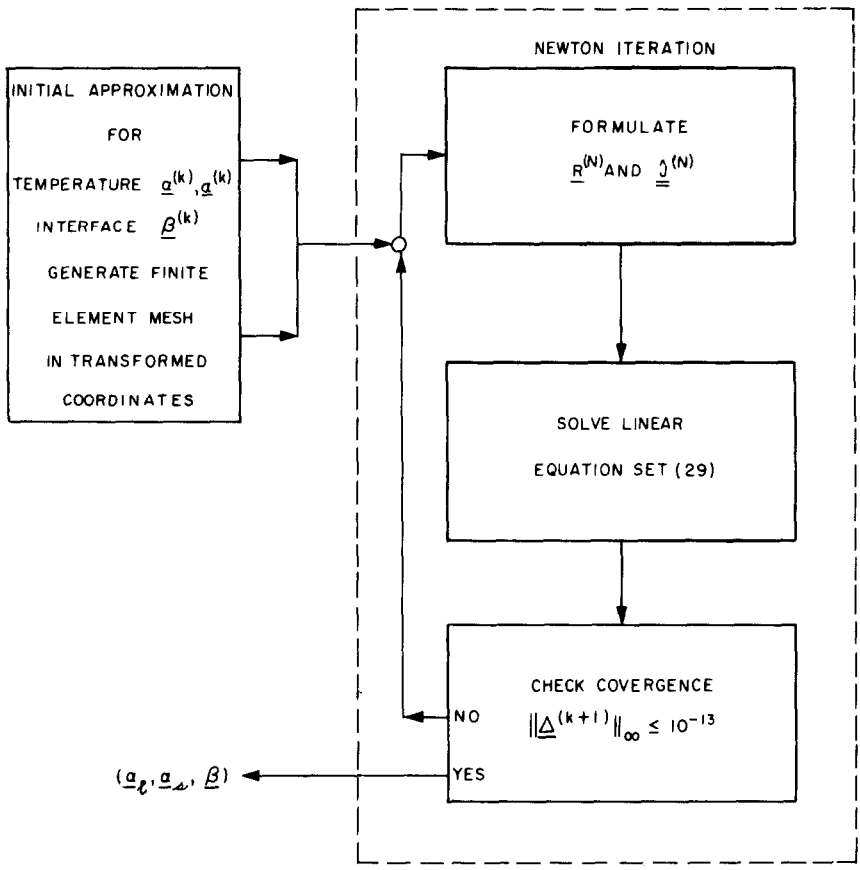

FIG. 9. Flowsheet for Isotherm–Newton method.

equations (29) while accounting for this structure. The Newton iterations are continued until the largest change in any component of $\Delta^{(k+1)}$ is less than 10^{-13}. This method is shown schematically in Fig. 9.

3.2c *Energy–Flux Method*

The finite-element representations for melt and solid temperature are best left separated when energy balance (3) at the interface is applied as the distinguished condition. In terms of the transformed coordinates, these are

$$\begin{aligned}\hat{T}_\ell(\xi,\eta) &= \sum_{i=1}^{N_\ell'} \alpha_{i,\ell}\Phi^i(\xi,\eta) + \sum_{i=1}^{N_0} \alpha_{i,\ell}^e \Phi^i(\xi,\eta) + \sum_{i=1}^{N_I} \alpha_{i,\ell}^I \Phi^i(\xi,\eta),\\ \hat{T}_s(\hat{\xi},\hat{\eta}) &= \sum_{i=1}^{N_s} \alpha_{i,s}\Phi^i(\hat{\xi},\hat{\eta}) + \sum_{i=1}^{N_0} \alpha_{i,s}^e \Phi^i(\hat{\xi},\hat{\eta}) + \sum_{i=1}^{N_I} \alpha_{i,s}^I \Phi^i(\hat{\xi},\hat{\eta}),\end{aligned} \tag{31}$$

where $N_\ell' \equiv N_\ell - N_I$ is the number of basis functions that are nonzero along the melt/solid boundary $\eta = L/2$. Isotherm condition (4) is satisfied as a boundary condition for *any* interface shape and the coefficients $\{\alpha_{i,\ell}^I\}$ and $\{\alpha_{i,s}^I\}$ are each equal to T_m. Expression (22b) represents $h(x)$.

The Galerkin equations for energy balance (2) are

$$\text{melt:} \quad R_{\ell,j}^{(F)} \equiv -\int_{\hat{\mathscr{D}}_\ell} [\hat{\nabla}_\ell \Phi^j \cdot \hat{\nabla}_\ell \hat{T}_\ell + \Phi^j P(\mathbf{e}_y \cdot \hat{\nabla}_\ell \hat{T}_\ell)](2h/L)\, d\xi\, d\eta$$

$$- \int_{\partial\hat{\mathscr{D}}_{1,\ell}} \Phi^j [B(\hat{T}_\ell - \hat{T}_\infty) + R(\hat{T}_\ell^4 - T_\infty^4)](2h/L)\, d\eta = 0,$$

$$j = 1,..., N_\ell', \quad (32)$$

$$\text{solid:} \quad R_{s,j}^{(F)} \equiv -\int_{\hat{\mathscr{D}}_s} [\hat{\nabla}_s \Phi^j \cdot \hat{\nabla}_s \hat{T}_s + \Phi^j P(\mathbf{e}_y \cdot \hat{\nabla}_s \hat{T}_s)](2/L)(L-h)\, d\xi\, d\eta$$

$$- \int_{\partial\hat{\mathscr{D}}_{1,s}} \Phi^j [B(\hat{T}_s - T_\infty) + R(\hat{T}_s^4 - T_\infty^4)](2/L)(L-h)\, d\eta = 0,$$

$$j = 1,..., N_s'. \quad (33)$$

The notation for regions and boundaries is given in Fig. 5.

The shape of the melt/solid interface is determined from the Galerkin residual equations for interfacial energy balance (3)

$$R_{I,j}^{(F)} \equiv \int_0^1 \Psi^j(\xi) \left(\mathbf{n} \cdot \hat{\nabla}_\ell T_\ell - \mathbf{n} \cdot \hat{\nabla}_s \hat{T}_s - \frac{PS}{[1 + h_x^2]^{1/2}} \right) ds = 0, \qquad j = 1,..., M. \quad (34)$$

Equations (32)–(34) together with expansions (22b) and (31) describe a system of $(N_s + N_\ell' + M)$ nonlinear algebraic equations in terms of the unknowns $(\boldsymbol{\alpha}_\ell, \boldsymbol{\alpha}_s, \boldsymbol{\beta})$. These equations are only partially coupled; the interface shape $h(x)$ appears in each equation, however, Galerkin equations (32) are independent of $\boldsymbol{\alpha}_s$ and Eqs. (33) are independent of $\boldsymbol{\alpha}_\ell$.

An attempt was made to decouple the equation set. For an approximate interface shape $\{\beta_i^{(k)}\}$, we solved Eqs. (32) for the temperature coefficients $\{\alpha_{\ell,i}\}$ and Eqs. (33) for $\{\alpha_{s,i}\}$. These temperature fields were used in the M equations of (34) to calculate an improved location for the phase boundary. Newton's method was employed for solving all three equations sets. This iterative scheme failed. Just as in the original coordinate system, the Jacobian matrix associated with the residual equations of the interfacial energy balance was numerically singular; the corrections to the interface location had sinusoidal oscillations that propagated with each iteration and caused the calculation to diverge. These oscillations were present even when the exact (to machine accuracy) interface shape was used as an initial approximation.

Solution of the entire equation set (32)–(34) by Newton's method was successful and is the basis for the Energy–Flux method. The system of linear equations solved at each iteration is

$$\hat{\underline{\underline{J}}}^{(F)}\Delta^{(k+1)} \equiv \begin{pmatrix} \hat{\underline{\underline{H}}}^{(\ell)} & \underline{\underline{0}} & \hat{\underline{\underline{G}}}^{(\ell)} \\ \underline{\underline{0}} & \hat{\underline{\underline{H}}}^{(s)} & \hat{\underline{\underline{G}}}^{(s)} \\ \hat{\underline{\underline{K}}}^{(\ell)} & \hat{\underline{\underline{K}}}^{(s)} & \hat{\underline{\underline{K}}}^{(I)} \end{pmatrix} \begin{pmatrix} \boldsymbol{\alpha}_\ell^{(k)} - \boldsymbol{\alpha}_\ell^{(k+1)} \\ \boldsymbol{\alpha}_s^{(k)} - \boldsymbol{\alpha}_s^{(k+1)} \\ \boldsymbol{\beta}^{(k)} - \boldsymbol{\beta}^{(k+1)} \end{pmatrix} = \begin{pmatrix} \mathbf{R}_\ell^{(F)} \\ \mathbf{R}_s^{(F)} \\ \mathbf{R}_I^{(F)} \end{pmatrix} \equiv \mathbf{R}^{(F)}. \tag{35}$$

The seven matrices appearing in the Jacobian $\hat{\underline{\underline{J}}}^{(F)}$ have components

$$\hat{H}_{ij}^{(\ell)} \equiv \partial R_{\ell,i}^{(F)}/\partial \alpha_{\ell,j}, \qquad i = 1,\ldots,N_\ell', \quad j = 1,\ldots,N_\ell', \tag{36a}$$

$$\hat{H}_{ij}^{(s)} \equiv \partial R_{s,i}^{(F)}/\partial \alpha_{s,j}, \qquad i = 1,\ldots,N_s', \quad j = 1,\ldots,N_s', \tag{36b}$$

$$\hat{G}_{ij}^{(\ell)} \equiv \partial R_{\ell,i}^{(F)}/\partial \beta_j, \qquad i = 1,\ldots,N_\ell', \quad j = 1,\ldots,M, \tag{36c}$$

$$\hat{G}_{ij}^{(s)} \equiv \partial R_{s,i}^{(F)}/\partial \beta_j, \qquad i = 1,\ldots,N_s', \quad j = 1,\ldots,M, \tag{35d}$$

$$\hat{K}_{ij}^{(\ell)} \equiv \partial R_{I,i}^{(F)}/\partial \alpha_{\ell,j}, \qquad i = 1,\ldots,M, \quad j = 1,\ldots,N_\ell', \tag{36e}$$

$$\hat{K}_{ij}^{(s)} \equiv \partial R_{I,i}^{(F)}/\partial \alpha_{s,j}, \qquad i = 1,\ldots,M, \quad j = 1,\ldots,N_s', \tag{36f}$$

$$\hat{K}_{ij}^{(I)} \equiv \partial R_{I,i}^{(F)}/\partial \beta_j, \qquad i = 1,\ldots,M, \quad j = 1,\ldots,M. \tag{36g}$$

Explicit formulas are derived for each of the components of $\hat{\underline{\underline{J}}}^{(F)}$, which has the same structure as the matrix $\hat{\underline{\underline{J}}}^{(N)}$ (cf. Eq. (32)). The schematic of the Energy–Flux iteration is identical to Fig. 9. The iterations are continued until the largest change in any component of the correction vector $\Delta^{(k)}$ is less than 10^{-13}.

4. Numerical Results

Fortran programs have been written for the four formulations of the solidification problem detailed in the previous section. Both linear and quadratic finite-element representations for temperature fields and melt/solid interface shape have been tested. All calculations were performed in extended precision arithmetic on the IBM 370/168 computer at the Massachusetts Institute of Technology.

The efficiency and accuracy of the four methods were compared for the case ($S = R = 0$), where the model problem became linear and the closed-form solution was known, and for cases where the nonlinearities caused by latent heat release ($S \neq 0$) and radiation ($R \neq 0$) were significant. The tests with the linear problem contrasted the accuracy of the various choices of finite element basis and *distinguished* condition, and gave indications of the relative efficiency of the four methods. This apparently linear test problem was *not* linear when viewed as a free-boundary problem in the framework of *any* of the four iterative schemes; multiple iterations were necessary for each scheme method to converge to the solution.

TABLE I

Comparison of Exact and Finite-Element Solutions for $B = 1.0$, $P = 0.5$, and $T_m = 0.5$

Solution method	Finite-element basis	Location of melt/solid interface $h(x)$					$\|\beta - \beta^e\|_2$	Execution time (cpu sec.)
		$x = 0$	$x = 0.25$	$x = 0.50$	$x = 0.75$	$x = 1.00$		
Exact solution	—	0.547364	0.542650	0.525413	0.488144	0.388702	—	—
Energy–flux	Linear	0.536874	0.536874	0.524418	0.491259	0.401754	1.91×10^{-2}	2.6
Isotherm	Linear	0.549118	0.544659	0.528042	0.487164	0.390716	5.21×10^{-3}	1.35
Kinematic–isotherm	Linear	0.549118	0.544659	0.528042	0.487164	0.390716	5.21×10^{-3}	2.7
Isotherm–Newton	Linear	0.549118	0.544659	0.528042	0.487164	0.390716	5.21×10^{-3}	2.5
Energy–flux	Quadratic	0.547407	0.542712	0.525511	0.484207	0.388723	2.31×10^{-4}	17.3
Isotherm	Quadratic	0.547341	0.542626	0.525378	0.484129	0.388656	8.05×10^{-5}	4.8
Isotherm–Newton	Quadratic	0.547341	0.542626	0.525378	0.484129	0.388656	8.05×10^{-5}	16.7

Note. All calculations were performed with a 4×4 grid of elements in both melt and solid.

The very nonlinear test problem substantiated the conclusions from the linear problem and pointed out the gain in efficiency due to the implementation of Newton's method for the simultaneous calculation of the field variables and free-boundary shape. All convergence results compare calculations that were initiated with the initial interface shape $h(x) = 0.5$ and with linear temperature profiles satisfying essential conditions (7).

4.1 *Comparison to Closed-Form Solution* ($R = S = 0$)

The melt/solid interface shapes generates by the four finite element methods are compared in Table I to the interface shape interpolated from the closed form of the temperature field for $R = 0$, $S = 0$, and $B = 1.0$. Results are given for a mesh of four quadrilateral elements in the x- and y-directions in both melt and solid regions. The finite-element results never differed from the exact solution by more than two percent.

Although the accuracy of the interface shape calculated by any of the methods was systematically improved by increasing the number of elements, the rate of improvement was found to be strongly dependent on the formulation and on the type of basis function employed. The change in the error in the computed interface shape with the characteristic size of the mesh is shown in Fig. 10 for the case $B = 0.1$. The error was measured by the norm of the difference between the coefficients $\{\beta_i\}$ of the finite-element approximation and the corresponding values $\{\beta_i^e\}$ interpolated from the exact temperature field

$$\|\boldsymbol{\beta} - \boldsymbol{\beta}^e\|_2 \equiv \left\{ \sum_{i=1}^{M} (\beta_i - \beta_i^e)^2 \right\}^{1/2}. \tag{37}$$

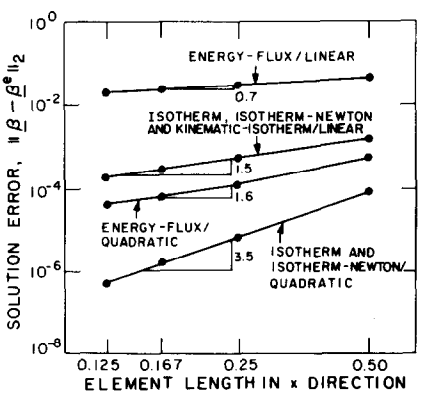

FIG. 10. Convergence of four finite-element formulations as a function of element size for prototype solidification problem with $B = 0.1$, $P = 0.5$, and $T_m = 0.5$. Results are shown for quadratic and linear bases.

Each curve in Fig. 10 was fit to the relationship

$$\|\beta - \beta^e\| = Ch^r \qquad (38)$$

rate for the formulations. These values of r are shown in Fig. 10. Several characteristics of the numerical formulations were apparent. As predicted from finite-element theory for the solution of linear partial differential equations [31], the quadratic polynomials were more accurate than the bilinear ones for bases formed from the same mesh. This result was independent of which formulation was used.

All three formulations based on melting point isotherm (4) as the *distinguished* condition had identical convergence rates. This was expected for the Kinematic–Isotherm and Isotherm–Newton formulations since both were based on the same set of residual equations. The equivalence of the interface shapes calculated by the Isotherm method and the two formulations in transformed coordiantes implied that the complications to the energy balances caused by mappings (8) and (9) did not reduce the accuracy of the calculated temperature fields. The values of r for bilinear ($r = 1.5$) and quadratic elements ($r = 3.5$) compared favorably with the values (bilinear $r = 2$, reduced quadratic $r = 3$) for solving linear equations [31] derived from asymptotic theories that are valid for small h. This agreement between calculations on relatively course grids and theory is not at all unusual for finite-element (or finite-difference) solution of elliptic equations with smooth solutions; for other examples see [31, Chap. 8; 32, Chap. 4].

The choice of distinguished boundary condition affected the accuracy of the formulation. The rates of convergence for the Energy–Flux formulation (based on the

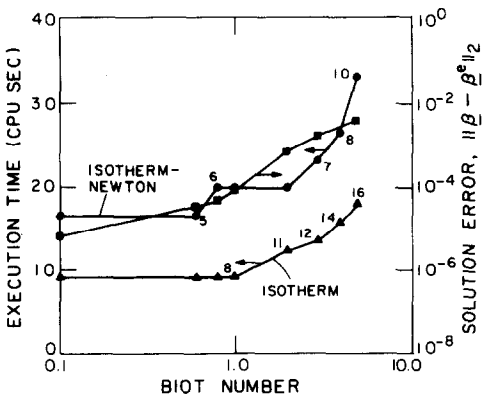

FIG. 11. Solution error and execution time as a function of Biot number B for $P = 0.5$ and $T_m = 0.5$. Results are for Isotherm and Isotherm–Newton formulations with a 4×4 mesh of elements in each phase and quadratic basis functions. The number of iterations required for each calculation is shown on the curve of execution times. For the same mesh, the errors in the solutions by the two methods are identical, since both are based on the same set of residual equations.

interfacial energy balance) were more than an order lower than the rates for the three methods based on the condition for interfacial equilibrium as the distinguished condition. The explanation for this result came from the form of the two interfacial boundary conditions. The energy balance required finite-element approximations to the normal derivatives of temperature at the interface; these derivatives are less accurate (at least one order of h) than the temperature fields needed in the isotherm condition.

The accuracy of the melt/solid interface shape computed by any of the finite-element formulations decreased with increasing Biot number; as B was increased, the phase boundary became more curved, the lateral temperature gradients increased and the temperature field calculation became more inaccurate. This trend is shown in Fig. 11 for the Isotherm–Newton and Isotherm formations with a 4×4 mesh of elements in each phase.

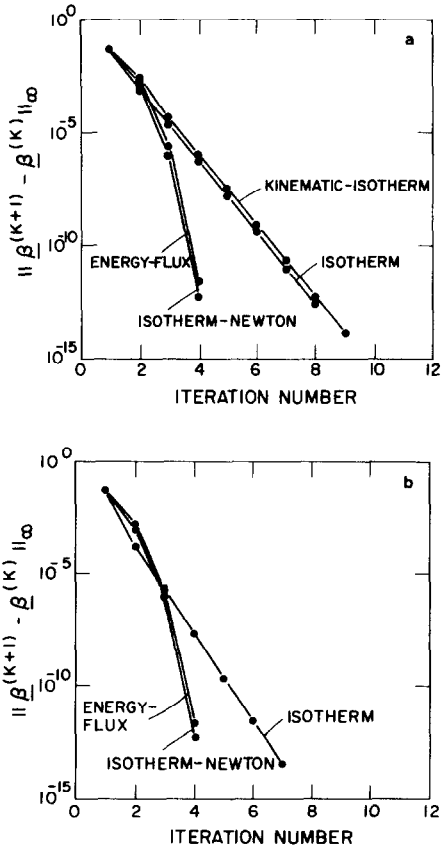

FIG. 12. Convergence of four formulations as a function of iteration number for $B = 0.1$, $P = 0.5$, and $T_m = 0.5$. Results are for (a) linear and (b) quadratic finite-element approximations and for a 4×4 mesh of elements in melt and solid.

The efficiency of each formulation is dependent on the choice of the iterative technique used to solve the set of nonlinear algebraic equations. Figures 12a and b show the convergence with iteration count for the four finite element approximations; the parameter values are the same as for Fig. 10. Convergence was measured by the magnitude of the largest change in the coefficients $\{\beta_i\}$ between two successive iterations, i.e.,

$$\|\boldsymbol{\beta}^{(k+1)} - \boldsymbol{\beta}^{(k)}\|_\infty \equiv \max_{i=1,\ldots,M} |\beta_i^{(k+1)} - \beta_i^{(k)}|. \tag{39}$$

The Energy–Flux and Isotherm formulations, both founded on Newton's method for solving the nonlinear equation set, exhibited quadratic rates of convergence (the number of significant digits in the approximate solution almost doubled from one iteration to the next), whereas both the Isotherm and Kinematic–Isotherm methods converged linearly.

The overall efficiency of each method accounts for the accuracy, rate of convergence, and computer time required for each iteration of the scheme. In Fig. 13, the accuracies of the calculated interface shape $\|\boldsymbol{\beta} - \boldsymbol{\beta}^e\|_2$ are plotted against the amounts of computer time (in cpu seconds) required for each of the four methods. For bilinear basis functions, the Isotherm and Kinematic–Isotherm methods had similar efficiency for a specified level of accuracy; no appreciable difference in execution time or accuracy was found between integrating numerically kinematic condition (33) or interpolating isotherm (27).

The quadratic convergence rate of the Isotherm–Newton method did not result in increased efficiency relative to the Isotherm and Kinematic–Isotherm formulations. For the Isotherm–Newton method, the large amount of execution time needed for inverting the matrix shown in Fig. 8 more than offset the fewer number of iterations

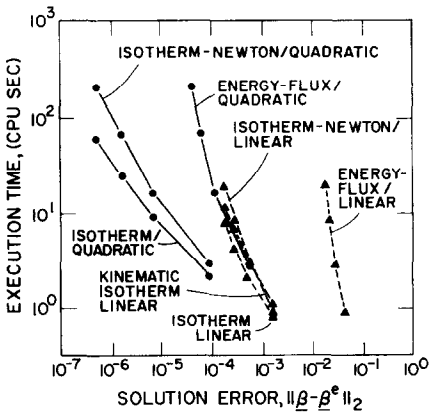

FIG. 13. Execution time as a function of error in the calculated melt/solid interface shape for $B = 0.1$, $P = 0.5$, and $T_m = 0.5$.

TABLE II

Melt/Solid Interface Shapes Calculated by the Isotherm, Isotherm–Newton, and Energy–Flux Methods with Three Finite-Element Grids for $R = 0.5$, $S = 1.0$, $B = 1$, $P = 0.5$, and $T_m = 0.5$

Solution method	Finite-element basis	Mesh	Location of melt/solid interface $h(x)$					Execution time (cpu sec.)
			$x = 0$	$x = 0.25$	$x = 0.50$	$x = 0.75$	$x = 1.00$	
Isotherm	Linear	4 × 4	0.657075	0.652852	0.636603	0.594482	0.484321	7.6
		6 × 6	0.656130	0.651125	0.635187	0.589521	0.481809	16.6
		8 × 8	0.655804	0.651394	0.634701	0.592252	0.480700	30.8
Isotherm	Quadratic	4 × 4	0.655355	0.650883	0.634035	0.591398	0.478690	36.5
		6 × 6	0.655380	0.650917	0.634074	0.591480	0.478339	124.4
		8 × 8	0.655384	0.650918	0.634082	0.591521	0.478181	292.3
Isotherm–Newton	Quadratic	4 × 4	0.655355	0.650883	0.634035	0.591398	0.478769	20.0
		6 × 6	0.655380	0.650917	0.634074	0.594800	0.478339	79.3
		8 × 8	0.655384	0.650918	0.634082	0.591521	0.478181	240.7
Energy–flux	Quadratic	4 × 4	0.655269	0.650768	0.633884	0.590921	0.478609	22.1
		6 × 6	0.655313	0.650819	0.633932	0.591144	0.478551	84.2
		8 × 8	0.655337	0.650859	0.633981	0.591313	0.478441	256.8

required by Newton's iteration. The Isotherm method was more efficient than the Isotherm–Newton method for calculations over nearly two decades of Biot number as shown in Fig. 11 along with the number of iterations for each calculation. The thermal problem defined by residual equations (19) for a specified interface shape was linear when $S = 0$ and $R = 0$; here, the Isotherm algorithm calculated an updated temperature field in a single Newton iteration. The Isotherm–Newton method was expected to be more efficient when the residuals of the field equations were nonlinear in the field variables, as is demonstrated by the results for the nonlinear solidification problem.

4.2 *Results for Nonlinear Solidification Problem*

The conclusions about the relative accuracy of the four finite-element schemes that were reached on the basis of the linear test problem remained unaltered when the nonlinearities caused by latent heat release and radiation from the side were included. Interface shapes are given in Table II for the Isotherm, Isotherm–Newton, and Energy–Flux methods with quadratic basis functions and the Isotherm method with linear ones. The results are for three meshes and $R = 0.5$ and $S = 1.0$. Underlined are the number of digits that remain unchanged relative to the most refined calculation for each method. Again the Isotherm and Isotherm–Newton formulations gave identical interface shapes and were more accurate than the Energy–Flux method. The rates of convergence of each formulation were estimated by using as the "exact" interface shape the result calculated with the Isotherm method for quadratic interpolation and an 8×8 mesh of elements in each phase. The norm of the difference between this interface shape and those calculated with other formulations is shown in Fig. 14 as a function of the characteristic element size. The relative accuracy of each

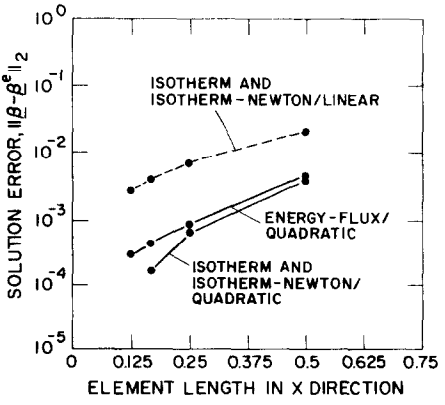

FIG. 14, Convergence of Isotherm, Isotherm–Newton, and Energy–Flux methods as a function of element size for $B = 1.0$, $R = 0.5$, $T_m = 0.5$, and $S = 1.0$.

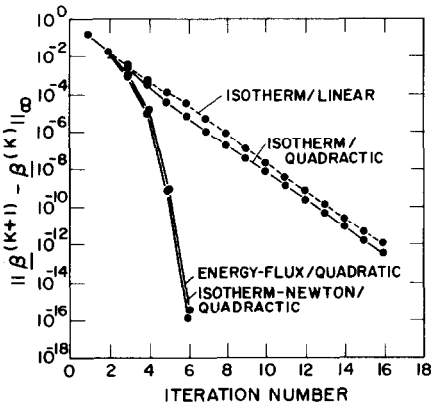

FIG. 15. Convergence of Isotherm, Isotherm–Newton, and Energy–Flux formulations as a function of iteration number for $R = 0.5$, $P = 0.5$, $S = 1.0$, $B = 1$, $T_m = 0.5$, $T_\infty = 0$, and $L = 1$. Results are for a 4×4 mesh of elements in each phase.

of the methods did not change with the addition of the nonlinearities caused by latent heat release and radiation; compare Figs. 10 and 14.

The convergence as a function of iteration number is shown in Fig. 15 for the

[redacted]

radiation ($R \neq 0$) made residual set (19) nonlinear in the coefficients for temperature, hence each iteration of the Isotherm scheme required one *or more* Newton iterations for calculation of an update to the temperature field. These additional iterations increased the execution time of the Isotherm iteration and, as expected, shifted its efficiency relative to the Isotherm–Newton and Energy–Flux formulations. As shown

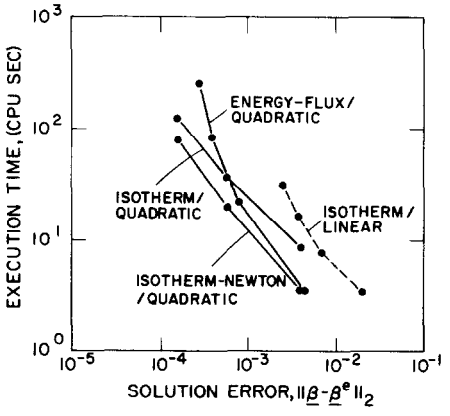

FIG. 16. Execution times as a function of error in the calculated melt/solid interface shape for the parameter values given in Fig. 15.

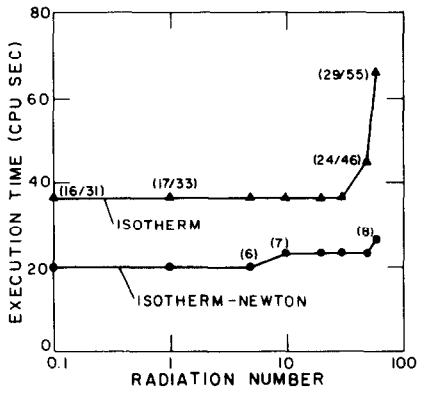

FIG. 17. Execution times for radiation numbers between 0.1 and 100 and for $P = 0.5$, $S = 1.0$, $B = 1.0$, $T_m = 0.5$, $T_\infty = 0$, and $L = 1.0$. Results are for a 4×4 mesh of elements in each phase. The number of iterations required for each calculation is shown above the curve. For the Isotherm method, the first coefficient is the number of overall iterations and the second is the number of Newton iterations for temperature fields.

in Fig. 16, the Isotherm–Newton formulation was found most efficient over a range of three decades of accuracy for the interface shape. The Energy–Flux method also was found to be competitive with the Isotherm formulation when the demands on solution accuracy were not stringent. The superior efficiency of the Isotherm–Newton method was found for the entire range of radiation numbers over which the formulations converged. The execution times for calculations performed with Isotherm and Isotherm–Newton formulations using quadratic basis functions are shown in Fig. 17. The number of iterations needed for each calculation is also shown; for the Isotherm scheme both the number of overall iterations and the total number of Newton

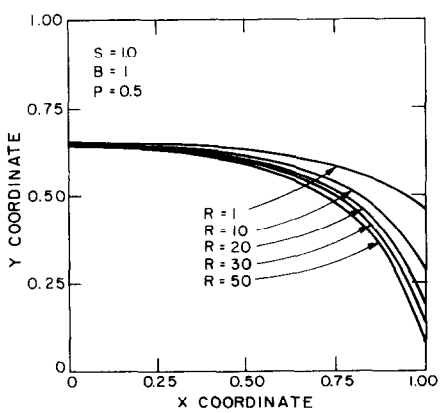

FIG. 18. Variation of melt/solid interface shape with radiation number.

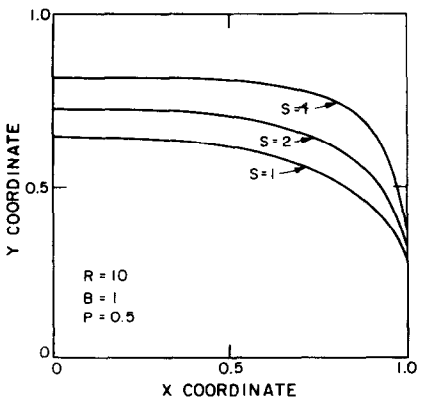

FIG. 19. Variation of melt/solid interface shape with latent heat release as measured by the Stefan number S.

iterations for the temperature field are shown. For radiation numbers between 0.1 and 10 the number of iterations required for convergence of the Isotherm–Newton algorithm stayed constant. As R was increased above ten, the melt/solid interface moved close to $y = 0$ and caused large temperature gradients in the melt; interface shapes for R between 1 and 50 are shown in Fig. 18. Neither the Isotherm nor the Isotherm–Newton iterations converged for R greater than 80 and the initial approximation of a flat phase boundary. No attempt was made to employ continuation methods to optimize the initial approximation and extend the range of R for convergence.

The rate of convergence of the Isotherm–Newton method was not affected by changes in the latent heat; for S between one and four this scheme converged quadratically in less than seven iterations. Interface shapes for three of these cases are

TABLE III

Comparison of Melt/Solid Interface Calculated by the Isotherm–Newton Method with $R = 10$, $S = 4.0$, $B = 1.0$, $P = 0.5$, and $T_m = 0.5$

Finite-element basis	Mesh	Location of melt/solid interface $h(x)$		
		$x = 0$	$x = 0.5$	$x = 1.0$
Linear	4×4	0.822997	0.810185	0.428789
	8×8	0.821231	0.808595	0.387874
	16×12	0.820717	0.808299	0.366873
Quadratic	4×4	0.820152	0.808117	0.386334
	8×8	0.820396	0.808305	0.365309

shown in Fig. 19. Increasing the amount of latent heat shifts the interface towards the cold end ($y = 1$) of the sheet and steepens the interface near the edge of the melt, thus causing large gradients in temperature. To better approximate these gradients, the quadrilateral mesh has been graded toward the interface in both melt and solid. This is easily done in the transformed coordinates (ξ, η) because the interface is the coordinate surface $\eta = \frac{1}{2}$. Interface positions calculated with both linear and quadratic basis functions and a number of meshes are shown in Table III. The shapes calculated with the linear and quadratic approximations were within ± 0.001 for the finest meshes used.

5. Conclusions

The Galerkin finite-element methods developed here are well suited to solving steady solidification problems. When the problem is solved in the original coordinate system, the unknown shape of the melt/solid interface is easily approximated by isoparametric finite elements and the flux boundary conditions are incorporated as natural conditions for the Galerkin residual equations. When the problem is transformed so that the interface becomes fixed, the flux conditions and field equations are complicated, but remain in gradient form so that they are systematically handled by Galerkin's method.

The choices of *distinguished* condition, of the technique used to solve the nonlinear algebraic equations, and of the finite-element basis all affect the accuracy and efficiency of the finite-element formulation. The choice of *distinguished* condition is critical. The three formulations based on the condition for interfacial equilibrium all produced more accurate interface shapes than the one method (Energy–Flux) that used the interfacial energy balance. Other formulations (III and IV in Fig. 1) based on the interfacial energy balance failed to converge for the prototype problem. The Isotherm and Kinematic–Isotherm formulations, like previous methods, decouple the calculation of the temperature field and interface shape at each iteration. When the energy equations (or boundary conditions) are nonlinear, iterative calculation of the temperature field is also needed. The Isotherm–Newton and Energy–Flux methods couple together the residuals of the field equations and the *distinguished* condition and iterate by Newton's method simultaneously for the interface shape and temperature field. Both methods converged in fewer iterations than the successive-approximation based formulation. When radiation and latent heat are included, the Isotherm–Newton formulation was most efficient because it combined the accuracy found in methods based on *distinguishing* the interfacial equilibrium condition with the rapid convergence of Newton's method. The Isotherm–Newton method converged for larger parameter ranges ($0 \leqslant R \leqslant 80$, $0 \leqslant S \leqslant 4$) than have been reported previously for any calculation of a Stefan problem.

The formulations and the conclusions reached about choices of *distinguished* condition and iteration scheme are applicable to models of solidification that are much more complicated than the problem treated here. Expanding the calculation to

include either a detailed model of the fluid mechanics in the melt [33] or the effect of mass transfer of a solute on the solidification of a binary melt [34] shifts the efficiency further towards the Isotherm–Newton scheme. Both cases result in much larger systems of algebraic equations for the field variables, i.e., temperature, velocity, pressure, and concentration, so that the number of coefficients associated with the interface shape is small compared to the number associated with the field variables. In these cases the additional cost is small for solving linear equation sets with the "arrowhead" structure over the banded matrices arising in successive approximation methods. Saito and Scriven [35] have reached this same conclusion for the calculation of a viscous flow with a meniscus by a Galerkin–Newton method. Although Saito and Scriven formulated the Galerkin equations in the original coordinate system, the residuals and elements of the Jacobian matrix were calculated in the transformed coordinates that correspond to the standard isoparametric mapping for each element [36]. The isoparametric mapping makes explicit the dependence of the nodes of the mesh and the basis functions on the interface shape and leads to formulas for the terms involving the interface shape in the Jacobian matrix. The isoparametric mapping technique is a method for implementing algorithms II and IV of Fig. 1.

ACKNOWLEDGMENTS

This research was supported in part by the Materials Processing in Space Program of the U.S. National Aeronautics and Space Administration, by a DuPont Young Faculty to R. A. B., and by the Information Processing Services at Massachusetts Institute of Technology. A summary of this paper was presented at the Fifteenth International Congress on Theoretical and Applied Mechanics, Toronto, August 1980.

REFERENCES

1. M. C. FLEMINGS, "Solidification Processing," McGraw–Hill, New York, 1974.
2. S. R. CORIELL AND R. F. SEKERKA, *J. Cryst. Growth* **46** (1979), 479.
3. P. G. KROEGER AND S. OSTRACH, *Int. J. Heat Mass Transfer* **17** (1974), 1191.
4. L.-C. TIEN, PH. D. THESIS, University of Michigan, Ann Arbor, 1968.
5. A. VALLE, PH. D. THESIS, University of Michigan, Ann Arbor, 1979.
6. G. H. MEYER, *SIAM J. Numer. Anal.* **10** (1973), 522.
7. N. SHAMSUNDAR AND E. M. SPARROW, *J. Heat Transfer* **97** (1975), 333.
8. H. G. LANDAU, *Quart. Appl. Math.* **8** (1950), 81.
9. F. W. SPAID, A. F. CHARWAT, L. G. REDEKOPP, AND R. ROSEN, *Int. J. Heat Mass Transfer* **14** (1971), 673.
10. J. L. DUDA, N. F. MALONE, R. H. NOTTER, AND J. S. VRENTAS, *Int. J. Heat Mass Transfer* **18** (1975), 901.
11. T. SAITOH, *Trans. ASME, J. Heat Transfer* **100** (1978), 294.
12. J. CRANK AND R. S. GUPTA, *Int. J. Heat Mass Transfer* **18** (1975), 1101.
13. J. CRANK AND A. B. CROWLEY, *Int. J. Heat Mass Trasnfer* **21** (1978), 393.
14. J. CRANK AND T. OGIS, *J. Inst. Math. Its Appl.* **26** (1980), 77.

15. G. H. MEYER, *J. Inst. Math. Its Appl.* **20** (1977), 317.
16. G. H. MEYER, *SIAM J. Numer. Anal.* **18** (1981), 150.
17. G. H. MEYER, *Numer. Heat Transfer* **1** (1978), 351.
18. G. H. MEYER, *Numer. Math.* **29** (1978), 329.
p. 167, Tokyo, 1976.
20. R. BONNEROT AND P. JAMET, *J. Comput. Phys.* **25** (1977), 163.
21. P. JAMET, *SIAM J. Numer. Anal.* **15** (1978), 912.
22. A. B. CROWLEY, *J. Inst. Math. Its Appl.* **24** (1979), 43.
23. D. R. LYNCH AND W. G. GRAY, *J. Comput. Phys.* **36** (1980), 135.
24. J. M. ORTEGA AND W. C. RHEINBOLDT, "Iterative Solution of Nonlinear Equations in Several Variables," Academic Press, New York, 1970.
25. R. A. BROWN, L. E. SCRIVEN, AND W. J. SILLIMAN, *in* "New Approaches in Nonlinear Dynamics" (P. J. Holmes, Ed.), SIAM, Philadelphia, 1980.
26. K. V. RAVI, *J. Cryst. Growth* **39** (1977), 1.
27. H. M. ETTOUNEY AND R. A. BROWN, *J. Cryst. Growth* **58** (1982), 313.
28. W. J. SILLIMAN AND L. E. SCRIVEN, *J. Comput. Phys.* **34** (1980), 287.
29. H. M. ETTOUNEY, PH. D. THESIS, Massachusetts Institute of Technology, Cambridge, 1982.
30. R. ARIS, "Vectors, Tensors, and the Basic Equations of Fluid Mechanics," Prentice–Hall, Englewood Cliffs, N.J., 1962.
31. G. STRANG AND G. J. FIX, "An Analysis of the Finite Element Method," Prentice–Hall, Englewood Cliffs, N.J., 1973.
32. B. A. FINLAYSON, "Nonlinear Analysis in Chemical Engineering," McGraw–Hill, New York, 1980.
33. C. J. CHANG AND R. A. BROWN, Buoyancy-driven convection near a melt/solid phase boundary, *in* "Proceedings, Second National Symposium on Numerical Methods in Heat Transfer," Maryland, to appear.
34. L. H. UNGAR, H. M. ETTOUNEY, AND R. A. BROWN, *Acta Metal.*, submitted.
35. H. L. SAITO AND L. E. SCRIVEN, *J. Comput. Phys.* **42** (1981), 53.
36. K. J. BATHE AND E. L. WILSON, "Numerical Methods in Finite Element Analysis," Prentice–Hall, Englewood Cliffs, N.J., 1976.